Nuclear Inst. and Methods in Physics Research, A 944 (2019) 162549

Contents lists available at ScienceDirect

Nuclear Inst. and Methods in Physics Research, A

journal homepage: www.elsevier.com/locate/nima

Quantitative analysis of NaI(Tl) gamma-ray spectrometry using an artificial neural network

Jinhwan Kim [a], Kyung Taek Lim [a], Junhyeok Kim [a], Chang-jong Kim [a,b], Byoungil Jeon [a,c], Kyeongjin Park [a], Giyoon Kim [a], Hojik Kim [a], Gyuseong Cho [a,*]

[a] Department of Nuclear & Quantum Engineering, Korea Advanced Institute of Science and Technology, Republic of Korea
[b] Nuclear Energy and Environment Research Laboratory, Korea Atomic Energy Research Institute, Daejeon 34507, Republic of Korea
[c] Neutron Science Center, Korea Atomic Energy Research Institute, Daejeon 34507, Republic of Korea

ABSTRACT

In this manuscript, we propose an algorithm based on an artificial neural network (ANN) for the analysis of the NaI(Tl) gamma-ray spectra with radioisotope (RI) mixtures to identify RIs and determine the relative activity levels of the identified RIs. The ANN was trained based on the spectra that were generated by synthesizing previously identified spectra from single RIs, considering the characteristics of the measurement environments, such as gain shift effects and statistical fluctuations in the spectrum. The proposed ANN was evaluated through several measured spectra that contained up to six certified reference materials for a quantitative analysis. We also evaluated the shift in the spectra due to temperature variations in the range of 0–50 °C and the low-count spectra with a one-second acquisition period. These results were compared with those from an ANN trained through simulated spectra to emphasize the importance of acquiring a high-quality training dataset. In addition, we show that complex low-resolution spectra can be accurately analyzed with the proposed ANN under various scenarios, in which the maximum root mean square error was found to be 2.8%.

1. Introduction

Radioisotope (RI) identification algorithms aim to identify or quantify radioactive materials by measuring the energy of the emitted gamma rays. Various fields such as homeland security, decontamination, nuclear nonproliferation, radioactive waste, and other disciplines that involve radiation rely on different types of detectors with dedicated algorithms to identify nuclear threats and to track and investigate radioactive materials. High-purity germanium (HPGe) detectors with high energy resolutions can provide an accurate quantitative analysis. However, these types of detectors are typically bulky because they require a cooling system to reach the cryogenic temperatures necessary for successful operation. Although portable HPGe detectors have been used in recent years, their high cost and low detection efficiency make them difficult to use in many practical applications. Thallium-doped sodium iodide (NaI(Tl)) detectors are also commonly used and can be manufactured in various forms, offering high detection efficiency. However, a quantitative analysis with these types of detectors remain challenging owing to their low energy resolutions and high sensitivity to temperature changes. Various RI algorithms have been proposed to overcome these limitations.

Wavelet analysis has been applied to the NaI(Tl) spectra to localize the photo-peaks to determine the gamma-ray energies of RIs [1]. The multiple-isotope material basis set method has been suggested to analyze spectra that have been attenuated and distorted by intervening absorbers [2,3]. A fuzzy-logic-based algorithm with feature extraction and pattern recognition capabilities has been applied to spectra that were measured for a short acquisition period [4]. A Bayesian-based algorithm has also been introduced to infer the posterior probability of RIs considering the factors such as the percentage of identified peaks, the centroid positions of the peaks, and the peak areas, thus yielding a list of RIs with detection certainties [5,6]. However, these methods are limited only to determining RI types in the sample at hand, and they cannot provide quantified information about activities. To enable quantitative analyses of low-resolution spectra, a genetic algorithm (GA) has been used to optimize the objective function, which is defined as a linear combination of the previously identified spectra of various single RIs (base spectra) to find a scale factor corresponding to each RI [7]. To improve the analysis performance, GAs have been combined with other techniques. One combination used multiple objectives and the Pareto optimality theory to enable the GA to search more extensively for a solution [8]. Another combination used fuzzy logic to detect possible RIs, and only these confined RIs were sent to the input of the GA [9]. Although these hybrid approaches are promising when used to analyze the relative activities of RIs with acceptable accuracy levels, actual spectra should be analyzed while considering other ambient conditions, such as the gain shift effect due to temperature changes. An artificial neural network (ANN) has been applied to low-resolution spectra to analyze complex spectra quantitatively considering poor statistics and gain shift effects [10–12]. This approach showed clear improvements over the earlier methods in terms of RI identification

* Corresponding author.
E-mail address: gscho@kaist.ac.kr (G. Cho).

https://doi.org/10.1016/j.nima.2019.162549
Received 4 April 2019; Received in revised form 18 July 2019; Accepted 7 August 2019
Available online 12 August 2019
0168-9002/

with a large number of RIs. Although researchers thus far have provided quantification analysis results of complex spectra with mixed RIs, most spectra were not obtained experimentally but were rather created via Monte Carlo simulations. In addition, the quantitative accuracy levels of the results need to be improved.

In this work, we propose an ANN-based algorithm that analyzes low-resolution gamma-ray spectra to provide identified RIs quantitatively in terms of their relative activity levels. Although previous studies have also presented methods based on ANNs with the same goal, we emphasize the importance of acquiring high-quality training data by comparing the ANN model trained by widely used simulated spectra with a model trained by the proposed measurement-based synthetic spectra. Through a data analysis, we demonstrate that the proposed model yields higher accuracy in comparison to that of a model trained by simulated spectra with respect to the measured complex spectra containing RI mixtures. Furthermore, we show that the proposed model is less vulnerable to shifts in the spectra and to low counts due to temperature variations and short acquisition periods, respectively.

2. Materials and methods

2.1. Artificial neural network

An ANN is a mathematical model that simulates the network of neurons in the brain so that a computer can learn things and make decisions in a humanlike manner. ANNs have been used in various fields in relation to radiation detection, such as dosimetry, pulse shape discrimination, and medical imagery [13–15]. Fig. 1 shows one example of an ANN architecture that consists of layers fully connected to each other. This ANN has L neurons in input layer A, M neurons in hidden layer B, and N neurons in output layer C. The neurons in the layers are next to each other and are connected by weights. Mathematical operations are performed in each neuron, summing the products of the values in the previous layer and the corresponding weight connecting the neurons, as shown in Fig. 2. This summation is then transformed by applying a nonlinear activation function, with the output then sent to the next layer. Typical choices of the activation function are the sigmoid, tanh or rectified linear unit (ReLU). The ANN may be trained so that the weights are adjusted to minimize the error of the cost function that evaluates the deviation of the output of the ANN from the true value. A common choice when training the ANN is backpropagation [16]. Backpropagation tracks the derivatives of the activation functions in each successive neuron to find the optimal weights that minimize the error. Various techniques that efficiently perform backpropagation have been suggested. In this paper, the Adam optimizer is chosen due to its overall performance capabilities [17]. With regard to the cost function, the cross-entropy function used in previous studies is applied here for error comparison purposes [10,11]. This is expressed as

$$\mathrm{E} = -\frac{1}{N}\sum_{n=1}^{N} y_n \log\left(\hat{y}_n\right) + \left(1 - y_n\right)\log\left(1 - \hat{y}_n\right), \tag{1}$$

where N is the total number of output neurons, y_n is the truth of the nth output, and $\hat{y}_n$ is the ANN output of the nth output.

Overfitting is a common problem for an ANN and can arise here due to the large number of parameters in this model. To address this issue, neuron dropout and early stopping are applied when training the model [18]. Dropout is a regularization technique that approximates the training of a large number of neural networks in parallel with different architectures. During each training iteration, some number of layer output (dropout rate) is ignored or dropped out at random. Therefore, dropout forces the learning algorithm to spread out the weights rather than letting it focus on specific features. Early stopping is another technique for improving generalization. In this method, the available data is divided into two subsets. The first subset is the training set, which is used to find the optimal weights in the layers.

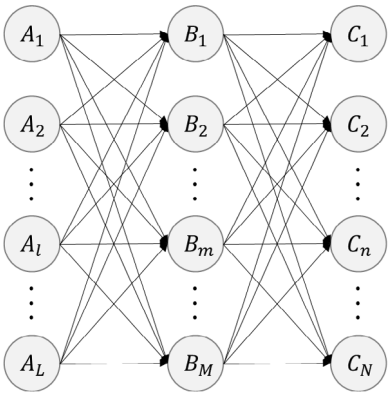

Fig. 1. An example of an ANN architecture with L neurons in input layer A, M neurons in hidden layer B, and N neurons in output layer C.

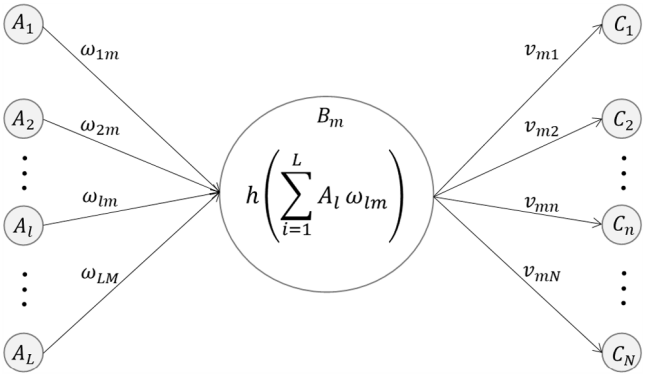

Fig. 2. Operation of a single neuron in hidden layer B.

The second subset is the validation set. The error of the validation set is monitored during the training process. In the initial stages of training, the validation error generally tends to decrease with the training error. However, the validation error begins to increase as the model starts to fit overly into the training data. Thus, terminating the training process around this time can prevent the overfitting issue. In this study, the training process was terminated when there was an increase in mean cross-entropy error of the validation set during 100 consecutive epochs. The ANN was modeled and trained through the Python package Keras, version 2.0.8, as the backend [19].

2.2. Establishment of the training and validation sets

Training and validation sets were created in two different ways for comparison purposes: one set consists of measurement-based synthetic spectra and the other consists of simulated spectra. The synthetic spectrum S can be assumed to be a linear combination of the base spectra, as follows,

$$S = \sum_{n=1}^{N} \varepsilon_{int,n} g_n r_n B_n, \tag{2}$$

where N is the population of RIs, $\mathcal{E}_{int,n}$ denotes the intrinsic efficiency, g_n is the gamma yield per decay (i.e., 2.797 $\gamma s^{-1} Bq^{-1}$ for the 511 and 1275 keV gamma-rays of ^{22}Na), r_n is the relative activity of the RIs, and B_n is the base spectrum for RI n retrieved from a base spectrum library that contains the following set: ^{152}Eu, ^{154}Eu, ^{22}Na, ^{54}Mn, ^{57}Co, ^{60}Co, ^{109}Cd, ^{133}Ba, and ^{137}Cs. The intrinsic efficiency was calculated via Monte Carlo N-Particle Transport Code 6 (MCNP6). To create the base spectrum library, each RI was measured for 600 s using a two-inch NaI(Tl) detector with the corresponding background

spectrum subtracted. The subtracted spectrum was then normalized to one. Although self-attenuation, pile-up, and shielding have effects on the measured spectral shape, these effects are assumed to be negligible. The detailed process of making the synthetic spectrum is shown in Fig. 3. Up to five random RIs were selected from the base spectrum library. The relative activity for the selected RIs was randomly sampled, while the others were assigned a value of zero. Then, the synthetic spectrum was made according to (2). To mimic the shift in the spectrum due to the gain shift effects, each channel in the spectrum was linearly repositioned. The shifted spectrum was reconstructed by means of spline interpolation with the original channels. The magnitude of this shift was randomly selected to be in the range of 0.92–1.08. This shifted spectrum does not reflect the features of the actual measured spectrum, such as the irreducible statistical fluctuations of the spectrum associated with physical processes. To mimic a more realistic spectrum, white noise was added and the spectrum was then normalized. This process was repeated to generate 100,000 and 10,000 spectra for the training and validation sets, respectively.

The simulated spectra were created using MCNP6. The methods used to select the RIs, the relative activity, and the magnitude of the shift in the spectrum was identical to those mentioned above. To consider different statistical fluctuations in the spectrum, the number of particle histories was randomly selected and was in the range of 1×10^4–1×10^7. Similar to the synthetic spectrum case, we simulated 100,000 and 10,000 spectra to generate the training set and the validation set, respectively. Fig. 4 shows the results of a comparison of the synthetic spectrum and the simulated spectrum with regard to the experimental spectrum with the following mixture configuration: ^{137}Cs, 39.0%; ^{22}Na, 30.5%; ^{60}Co, 23.5%; and ^{54}Mn, 7%. As shown in this figure, the synthetic spectrum mimics the measured spectrum better than the spectrum simulated. It should also be noted that the coefficients "a", "b", and "c" of the FT8 GEB card for the peak-broadening effect in the NaI(Tl) detector were optimized using a genetic algorithm to make the simulated spectrum resemble the experimental spectrum as much as possible [20], but these values still had some discrepancies in comparison to physical values.

2.3. Establishment of the test set

To create a test set, gamma spectra were measured with six combinations of RIs, as given in Table 1. The corresponding RIs were placed 6 cm away from the NaI(Tl) detector for 300 s at room temperature (20 °C). In this case, certified reference materials were used. Two more test sets were made by assuming low-count and gain-shift scenarios. The low-count scenario was intended to evaluate how well the proposed algorithm analyzes highly fluctuating spectra without obvious photo-peaks. Hence, spectra were made for the six cases with a one-second acquisition period. The gain-shift scenario was intended to ensure that accuracy is maintained when the spectra are shifted due to temperature changes. The most complex spectra with the mixture configuration of Case 6 was measured under conditions identical to those mentioned above but with the temperature increased from 0 to 50 °C in steps of 10 °C. At each step, the temperature was held for two hours to achieve equilibrium in the entire volume of the scintillator. It should be noted that the NaI(Tl) scintillator connected to a photomultiplier tube (PMT) was placed in a constant-temperature oven (HG-THC150), whereas nuclear instrumentation modules such as an amplifier (ORTEC 673) and a multi-channel analyzer (ORTEC TRUMP-PCI-2k) were placed outside of the oven at a constant room temperature. Fig. 5 shows the relative photo-peak positions of a ^{60}Co spectrum while adjusting the temperatures. In this figure, the spectrum slightly shifts in the positive direction, possibly because the light yield of the NaI(Tl) scintillators tends to fluctuate slightly as the temperature increases, whereas the PMT gain tends to decrease [21]. Although the spectrum rarely shifted in this case, it was intentionally biased toward the positive direction by adjusting the gain and was then measured for the gain-shift scenario.

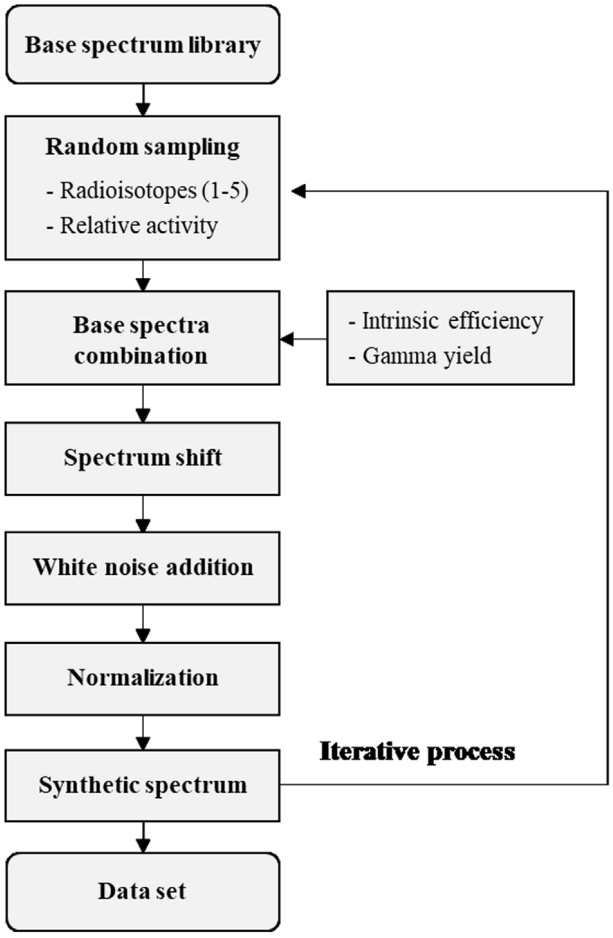

Fig. 3. A block diagram of the overall process used to create the synthetic spectrum.

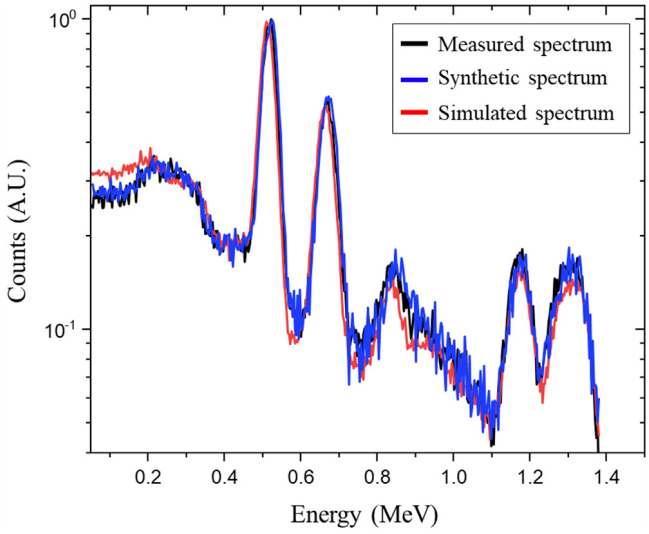

Fig. 4. A comparison of the synthetic spectrum and the simulated spectrum with respect to the measured spectrum for the following mixture: ^{137}Cs, 39.0%; ^{22}Na, 30.5%; ^{60}Co, 23.5%; and ^{54}Mn, 7.0%. The amount of shift in the synthetic and simulated spectra was set as unity.

2.4. Hyper-parameter optimization

The proposed ANN has several hyper-parameters that define the model architecture, including the number of layers, the number of

Table 1
Current activity of certified radioactive materials and six combinations of RIs for a test set.

RIs	Current activity (μCi)	Case					
		1	2	3	4	5	6
^{152}Eu	0.917	○	○	○	○	○	○
^{154}Eu	0.873		○		○	○	○
^{60}Co	0.743			○	○	○	○
^{137}Cs	0.953				○	○	○
^{22}Na	0.568			○		○	○
^{54}Mn	0.165						○
^{57}Co	0.125						
^{109}Cd	0.280						
^{133}Ba	0.923						

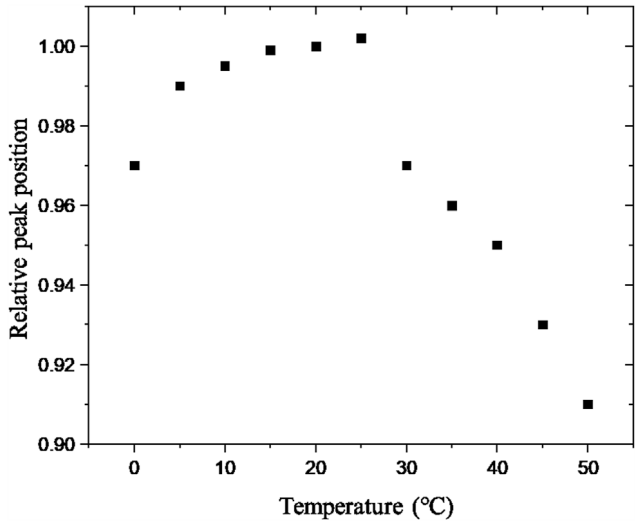

Fig. 5. Relative ^{60}Co peak position versus the temperature change of 0–50 °C.

neurons and the activation function of each layer, the learning rate of the Adam optimizer, the neuron dropout rate, and the batch size. These parameters cannot be trained directly from the training data and can significantly affect the performance of the ANN. Therefore, choosing the optimal hyper-parameters is crucial. One of the predetermined hyper-parameters is the softmax activation function,

$$\text{softmax}\left(z_j\right) = \frac{\exp\left(z_j\right)}{\sum_{n=1}^{N}\exp(z_n)}, \tag{3}$$

which is located in the last layer to quantify the probability linked to each output neuron. Although this function is traditionally used for classification, it is effective in a regression model [10–12]. The remaining hyper-parameters were determined using Bayesian optimization, which uses all available information from previous evaluations of the model to determine where to sample for the next evaluation, whereas the grid search and random search methods operate independently of the previous run [22,23]. Bayesian optimization consists of two main parts. First, it builds a statistical model f, which is a Gaussian process due to its flexibility and tractability for the objective function (that is, the cross-entropy function), after which it updates the posterior probability distribution of f using all available data. The mean and covariance matrices for the posterior distribution were calculated using the Matern 5/2 kernel function [22]. The acquisition function was then calculated using the current posterior distribution. Here, the expectation improvement was used to determine the next sampling point for the evaluation. We used Bayesian optimization as implemented in the Python package GpyOpt, version 1.2.0, which searched the space of the

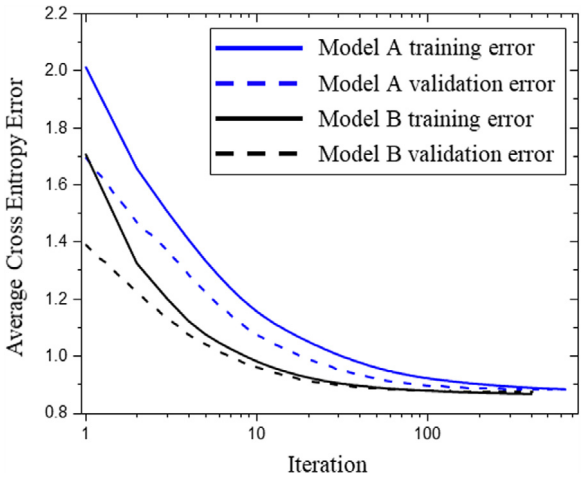

Fig. 6. The training error (solid line) and the validation error (dotted line) with optimal hyper-parameters searched by the Bayesian optimization process for Models A (blue) and B (black). (For interpretation of the references to color in this figure legend, the reader is referred to the web version of this article.)

hyper-parameters in Table 2. This table presents the optimized hyper-parameters for two models trained by the synthetic spectra (Model A) and trained by the simulated spectra (Model B). The errors with these optimized values during training are shown in Fig. 6. The training error calculations for both models were terminated just before the errors between the training and validation began to diverge from each other; i.e., neither model overfits the training data.

3. Results

3.1. Performance in a radioisotope analysis

To validate the performance of the two different models with regard to the quantitative analysis of the RIs, we quantified the RIs that contribute to the spectra as measured by the NaI(Tl) detectors for the test spectra of six cases (Table 1). For a direct comparison of the obtained results, a root mean square error (RMSE) was used, where

$$\text{RMSE}\ (\%) = \sqrt{\frac{\sum_{n=1}^{N}\left(y_n - \hat{y}_n\right)^2}{n}}. \tag{4}$$

RMSE, a metric used for model evaluations, represents the square root of the average squared differences between the expected value y_n and the predicted value $\hat{y}_n$. This metric assigns a relatively high weight to large differences that are undesirable. Fig. 7 shows the test spectrum of the six cases (red line) and the corresponding spectrum estimated based on the quantitative analysis results evaluated by Model A (blue dotted line). These results were compared to those evaluated by Model B, and their corresponding RMSE outcomes are given in Table 3. Although these spectra exhibit complex spectral shapes, Model A was able correctly to identify RIs on the spectra that contain up to six RIs and determine their relative activity levels with acceptable accuracy; the RMSE outcomes of Cases 1, 2, 3, 4, 5, and 6 were 0.0, 1.0, 1.6, 1.0, 0.9, and 1.8%, respectively. As presented in Fig. 7, their estimated spectra are in good agreement with the test spectra. Model B was also able to identify RIs in the test spectra, but it determined that there were additional RIs that did not contribute to the spectra. In addition, the RMSE outcomes of Cases 1, 2, 3, 4, 5 and 6 were 5.7, 15.3, 2.4, 6.1, 2.8, and 2.9%, respectively, showing inferior quantitative analysis results. However, when Model B evaluated simulated spectra with the same mixture configuration used with the six cases, it showed opposite results, as presented in Table 4. Model B accurately analyzed these

Table 2
Search spaces of the hyper-parameters and the corresponding optimal values for Models A and B.

Hyper-parameters	Search space	Type	Determined values	
			Model A	Model B
Number of layers	[1, 2, 3, 4]	Discrete	2	2
Learning rate	[10^{-1}, 10^{-5}]	Continuous	9.82×10^{-3}	2.84×10^{-4}
Batch size	[100, 500, 1000, 3000]	Discrete	500	3000
Activation function	[sigmoid, tanh, Relu]	Discrete	Relu	Relu
Neuron number in layer 1	[1, 10000]	Continuous	410	710
Dropout rate in layer 1	[0, 1]	Continuous	0.59	0.20
Neuron number in layer 2	[1, 10000]	Continuous	468	1454
Dropout rate in layer 2	[0, 1]	Continuous	0.63	0.37

Table 3
Comparison results of the quantitative analysis of the measured spectra of six cases with a 300 s acquisition period for Models A and B, and their corresponding RMSE values.

Case	Group		Radioisotopes									RMSE(%)
			^{152}Eu	^{154}Eu	^{60}Co	^{137}Cs	^{22}Na	^{54}Mn	^{57}Co	^{109}Cd	^{133}Ba	
1	Expected value		100.0	0.0	0.0	0.0	0.0	0.0	0.0	0.0	0.0	–
	Predicted value	Model A	100.0	0.0	0.0	0.0	0.0	0.0	0.0	0.0	0.0	0.0
		Model B	87.6	0.0	0.0	0.0	0.0	0.0	0.0	0.0	11.9	5.7
2	Expected value		51.2	48.8	0.0	0.0	0.0	0.0	0.0	0.0	0.0	–
	Predicted value	Model A	49.0	50.9	0.0	0.0	0.0	0.0	0.0	0.0	0.0	1.0
		Model B	29.6	32.3	0.0	0.0	0.0	0.0	0.0	37.0	1.0	15.3
3	Expected value		41.0	0.0	33.3	0.0	25.7	0.0	0.0	0.0	0.0	–
	Predicted value	Model A	37.2	0.0	36	0.0	26.9	0.0	0.0	0.0	0.0	1.6
		Model B	36.2	0.0	36.5	0.0	23.5	3.6	0.0	0.0	0.0	2.4
4	Expected value		26.3	25.0	21.4	27.3	0.0	0.0	0.0	0.0	0.0	–
	Predicted value	Model A	24.5	25.6	23.5	26.3	0.0	0.0	0.0	0.0	0.0	1.0
		Model B	20.4	21.4	19.2	22.4	0.0	0.0	0.0	16.0	0.0	6.1
5	Expected value		22.6	21.5	18.4	23.4	14.1	0.0	0.0	0.0	0.0	–
	Predicted value	Model A	22.2	22.2	19.6	24.1	12.0	0.0	0.0	0.0	0.0	0.9
		Model B	20.6	19.5	19.1	20.9	11.1	2.2	0.0	6.3	0.0	2.8
6	Expected value		21.7	20.7	17.6	22.5	13.6	3.9	0.0	0.0	0.0	–
	Predicted value	Model A	21.0	23.1	16.7	22.7	9.7	6.5	0.0	0.0	0.0	1.8
		Model B	20.1	18.7	17.5	19.5	10.9	6.5	0.0	6.6	0.0	2.9

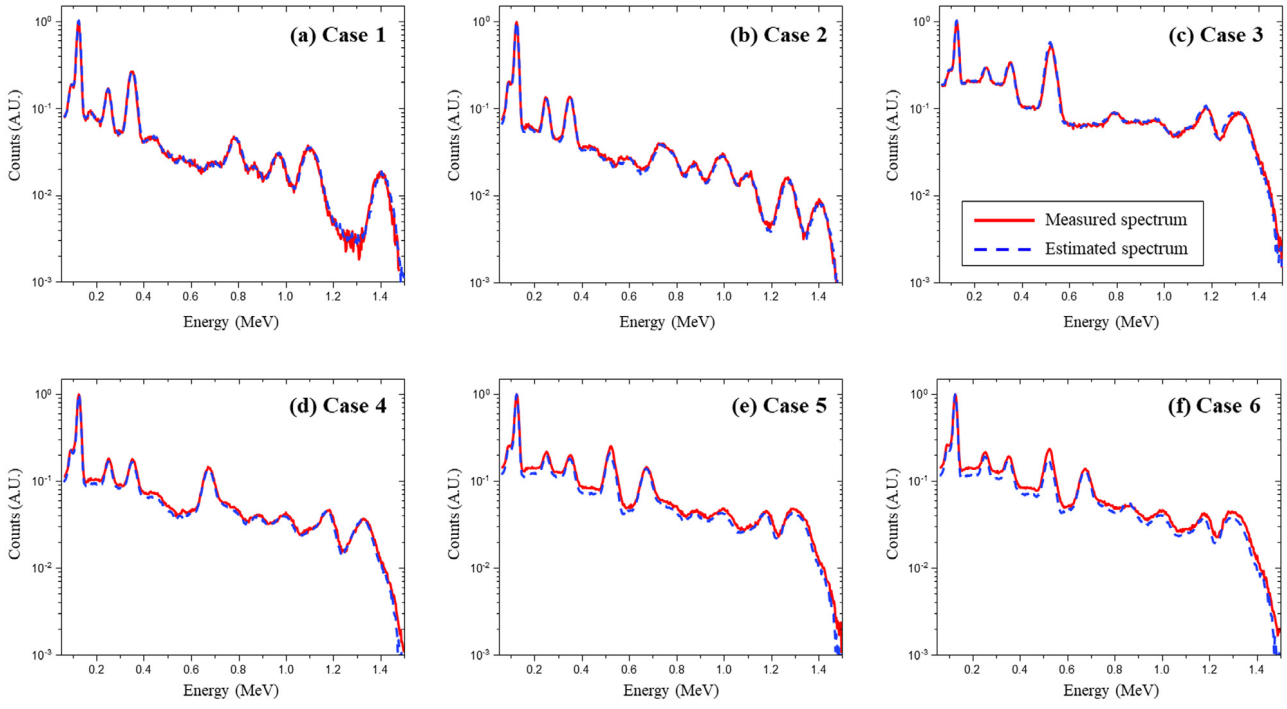

Fig. 7. The measured spectrum of six cases (red line) with a 300-second acquisition period against the spectrum estimated based on the analysis results as evaluated through Model A (blue dotted line)

simulated spectra, showing that the RMSE outcomes for Cases 1, 2, 3, 4, 5 and 6 were 0.0, 0.2, 0.4, 0.2, 0.4, and 0.9%, respectively, whereas Model A provided poor analysis results, with corresponding RMSE outcomes of Cases 1, 2, 3, 4, 5 and 6 of 0.0, 5.4, 1.0, 5.7, 5.3,

Table 4
Comparison results of the quantitative analyses of the simulated spectra with the same mixture configuration of the six cases for Models A and B, and their corresponding RMSE values.

Case	Group		Radioisotopes									RMSE (%)
			^{152}Eu	^{154}Eu	^{60}Co	^{137}Cs	^{22}Na	^{54}Mn	^{57}Co	^{109}Cd	^{133}Ba	
1	Expected value		100.0	0.0	0.0	0.0	0.0	0.0	0.0	0.0	0.0	–
	Predicted value	Model A	100.0	0.0	0.0	0.0	0.0	0.0	0.0	0.0	0.0	0.0
		Model B	100.0	0.0	0.0	0.0	0.0	0.0	0.0	0.0	0.0	0.0
2	Expected value		51.2	48.8	0.0	0.0	0.0	0.0	0.0	0.0	0.0	–
	Predicted value	Model A	62.4	37.3	0.0	0.0	0.0	0.0	0.0	0.0	0.0	5.4
		Model B	50.7	49.0	0.0	0.0	0.0	0.0	0.0	0.0	0.0	0.2
3	Expected value		41.0	0.0	33.3	0.0	25.7	0.0	0.0	0.0	0.0	–
	Predicted value	Model A	39.4	0.0	32.4	0.0	28.2	0.0	0.0	0.0	0.0	1.0
		Model B	40.2	0.0	34.0	0.0	25.7	0.0	0.0	0.0	0.0	0.4
4	Expected value		26.3	25.0	21.4	27.3	0.0	0.0	0.0	0.0	0.0	–
	Predicted value	Model A	30.7	10.9	22.7	35.6	0.0	0.0	0.0	0.0	0.0	5.7
		Model B	26.7	25.0	21.1	27.1	0.0	0.0	0.0	0.0	0.0	0.2
5	Expected value		22.6	21.5	18.4	23.4	14.1	0.0	0.0	0.0	0.0	–
	Predicted value	Model A	25.7	7.8	17.7	30.1	16.5	0.0	2.1	0.0	0.0	5.3
		Model B	22.5	20.9	19.1	24.0	13.4	0.0	0.0	0.0	0.0	0.4
6	Expected value		21.7	20.7	17.6	22.5	13.6	3.9	0.0	0.0	0.0	–
	Predicted value	Model A	23.1	11.2	15.8	28.5	15.8	5.5	0.0	0.0	0.0	3.9
		Model B	21.5	21.9	18.0	22.1	11.5	4.9	0.0	0.0	0.0	0.9

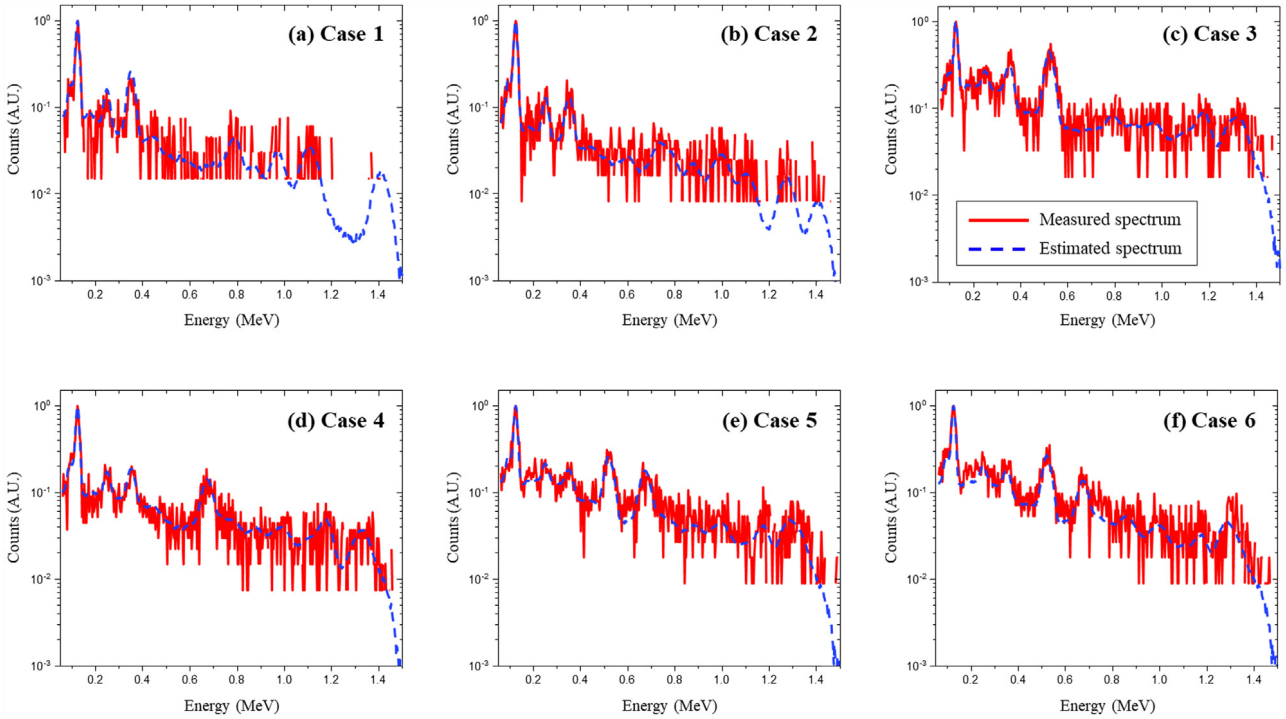

Fig. 8. The measured spectrum of six cases (red line) with a one-second acquisition period against the estimated spectrum based on the quantitative results evaluated through Model A (blue dotted line)

and 3.9%. These results stem from certain discrepancies between the spectra trained for the ANN and the spectra actually evaluated.

3.2. Performance on low-count spectra

To investigate how well the ANN analyzes highly fluctuating spectra without obvious photo-peaks, the spectra were measured for one second for the six cases. Fig. 8 illustrates the measured spectra (red line) and estimated spectra based on the quantitative analysis results evaluated via Model A (blue dotted line). These results were also compared to those evaluated via Model B. Despite the lack of obvious photo-peaks, Model A correctly identified RIs and provided activity levels nearly identical to the expected values; the RMSE outcomes of Cases 1, 2, 3, 4, 5, and 6 were 0.0, 1.4, 1.6, 1.9, 2.8 and 1.8%, respectively. These results demonstrate only a slight increase in the RMSE compared to the results obtained from the measured spectra in Fig. 7. This was made possible by the addition of various magnitudes of white noise to mimic the actual measured spectra with a short acquisition period when we synthesized the spectra for the training data. Model B was able to identify RIs, but it determined that there were additional RIs that are not part of the spectra. In addition, the RMSE outcomes of Cases 1, 2, 3, 4, 5, and 6 were 0.3, 5.6, 4.7, 12.7, 7.0, and 5.2%, respectively, showing a relatively large increase compared to the results acquired from the measured spectra in Fig. 7. From the comparison of the results of the two models, we confirmed that the ANN provides more degraded analysis results for highly fluctuating spectra when the training spectra are inconsistent with the measured spectra.

Table 5
Comparison results of the quantitative analyses of the measured spectra of six cases with a one-second acquisition period (low-count scenario) evaluated through Models A and B, and their corresponding RMSE values.

Case	Group		Radioisotopes									RMSE (%)
			^{152}Eu	^{154}Eu	^{60}Co	^{137}Cs	^{22}Na	^{54}Mn	^{57}Co	^{109}Cd	^{133}Ba	
1	Expected value		100	0.0	0.0	0.0	0.0	0.0	0.0	0.0	0.0	–
	Predicted value	Model A	100.0	0.0	0.0	0.0	0.0	0.0	0.0	0.0	0.0	0.0
		Model B	76.0	16.1	0.0	0.0	0.0	0.0	0.0	7.9	0.0	10.0
2	Expected value		51.2	48.8	0.0	0.0	0.0	0.0	0.0	0.0	0.0	–
	Predicted value	Model A	48.2	51.8	0.0	0.0	0.0	0.0	0.0	0.0	0.0	1.4
		Model B	24.7	36.9	0.0	0.0	0.0	0.0	0.0	33.4	4.5	14.8
3	Expected value		41	0.0	33.3	0.0	25.7	0.0	0.0	0.0	0.0	–
	Predicted value	Model A	37.2	0.0	36.0	0.0	26.9	0.0	0.0	0.0	0.0	1.6
		Model B	27.1	1.6	36.9	0.0	25.9	8.2	0.0	0.0	0.0	5.5
4	Expected value		26.3	25.0	21.4	27.3	0.0	0.0	0.0	0.0	0.0	–
	Predicted value	Model A	29.1	20.7	23.5	26.7	0.0	0.0	0.0	0.0	0.0	1.9
		Model B	19.3	21.2	21.3	21.8	0.0	3.5	0.0	12.6	0.0	5.4
5	Expected value		22.6	21.5	18.4	23.4	14.1	0.0	0.0	0.0	0.0	–
	Predicted value	Model A	17.8	21.0	16.5	29.9	14.3	0.0	0.0	0.0	0.0	2.8
		Model B	16.0	16.1	16.4	12.1	10.1	0.0	0.0	29.3	0.0	10.9
6	Expected value		21.7	20.7	17.6	22.5	13.6	3.9	0.0	0.0	0.0	–
	Predicted value	Model A	20.4	22.0	13.2	23.2	15.6	5.5	0.0	0.0	0.0	1.8
		Model B	19.9	18.6	14.5	18.3	12.4	4.0	0.0	12.0	0.0	4.5

3.3. Performance on gain shift

For a more in-depth analysis of the gain shift effects, the Case 6 spectra were evaluated while altering the temperature in the range of 0–50 °C in steps of 10 °C. Fig. 9 shows an example of the spectra measured at 20 °C (gray line) and at 50 °C (red line). In addition, this spectrum was evaluated when intentionally shifted in a positive direction (blue line). These shifted spectra would be difficult to analyze without recalibration because the positions of the original photo-peaks move to other photo-peak positions as the spectrum shifts. Furthermore, for the spectrum shifted in the positive direction, the spectrum is both shifted and further broadened. Nonetheless, Models A and B demonstrated some degree of temperature invariance, showing only a slight fluctuation of the RMSE, as shown in Table 6. This occurs because the training data were created while considering intentionally shifted spectra to minimize the positional effects of features, such as the photo-peaks, and to train the overall spectral shape. Although Model A incorrectly identifies ^{109}Cd in some spectra, the predicted value of the relative activities was insignificant (less than 1.0%). The incorrectly identified RI can be rejected by determining the minimum contribution threshold based on an analysis of the false alarm rate on the training set [10]. It should be noted that the quantitative analysis results evaluated by Model B remain consistently degraded.

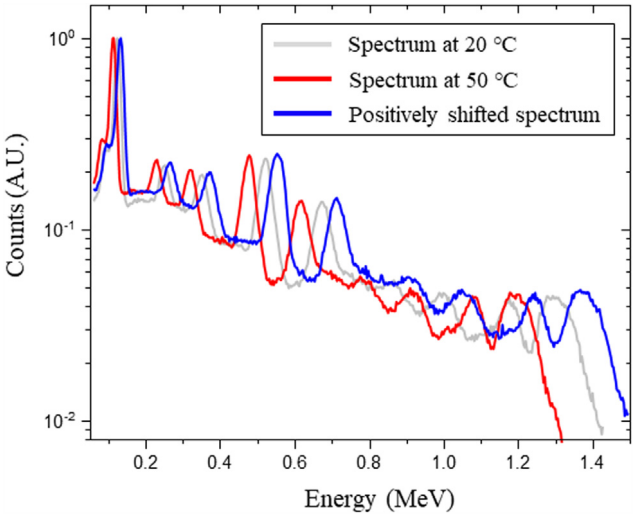

Fig. 9. Case 6 (^{152}Eu, ^{154}Eu, ^{60}Co, ^{137}Cs, ^{22}Na, ^{54}Mn) spectra measured at 20 and 50 °C, and the spectrum positively biased by adjusting the gain. (For interpretation of the references to color in this figure legend, the reader is referred to the web version of this article.)

4. Discussion

Here, we demonstrated an ANN-based algorithm to identify RIs in complex low-resolution NaI(Tl) spectra and determine the relative activities of the identified RIs. In particular, we compare a model trained with measurement-based synthetic spectra with a model trained with simulated spectra to emphasize the importance of acquiring high-quality training data. From the results, we confirmed that the model trained with the simulated spectra showed inferior performance in terms of RI identification and quantification under various scenarios (Table 3, 5, and 6) in comparison to those of the model trained with synthetic spectra, which were similar to the measured spectra (Fig. 1). This occurred because the simulated spectra used to create the training set had some discrepancies in comparison to the measured spectra (Table 4). In fact, previous studies used Monte Carlo simulations to mimic the measured spectra to generate the training set, and they performed the data analysis for simulated spectra with RI mixtures [10–12]. It should be noted that these results would have been further degraded if measured spectra were used for the evaluation. We are aware of the accessibility of the simulation process in terms of generating spectra and including additional RIs due to the challenges that may be encountered when measuring RIs (e.g., short half-lifetimes) for synthetic spectrum generation. Nonetheless, it is important to recognize that some discrepancies between the measured and simulated spectra can degrade the accuracy of the data analysis because it is difficult fully to mimic actual measured spectra through a simulation [20,24–27]. In fact, this problem may not be fully addressed in a manner that solves the overfitting issue, as it results from fundamental differences between the spectra used for the training set and those used for the test set.

We also showed how accurate results from a quantitative analysis of low-resolution spectra can be achieved. The proposed model was able fully to identify complex low-resolution spectra that contain up to six RIs even under the low-count and gain-shift scenarios (Table 3, 5, and 6), thus demonstrating clear improvements in comparison to previous cases [10–12]. This could be due to the high-quality training data used, as mentioned above, and to the limited number of target RIs. In contrast, previous studies included approximately 30 target

Table 6
Comparison results of the quantitative analyses of the measured spectra of Case 6 while changing the temperature in the range of 0–50 °C in steps of 10 °C evaluated through Models A and B, and their corresponding RMSE values.

Temp (°C)	Group		Radioisotopes									RMSE(%)
			^{152}Eu	^{154}Eu	^{60}Co	^{137}Cs	^{22}Na	^{54}Mn	^{57}Co	^{109}Cd	^{133}Ba	
Expected value			21.7	20.7	17.6	22.5	13.6	3.9	0.0	0.0	0.0	-
0	Predicted value	Model A	20.1	22.7	15.5	22.8	12.6	5.5	0.0	0.8	0.0	1.3
		Model B	18.8	18.0	15.9	18.5	10.6	6.6	0.0	10.1	1.5	4.2
10	Predicted value	Model A	19.9	22.5	15.3	21.8	14.2	6.2	0.0	0.0	0.0	1.4
		Model B	19.0	18.5	16.3	18.5	11.1	6.1	0.0	8.4	2.1	3.6
30	Predicted value	Model A	20.2	22.7	16.2	23.0	12	5.8	0.0	0.0	0.0	1.3
		Model B	18.7	17.9	16.0	18.6	10.5	6.6	0.0	10.2	1.3	4.2
40	Predicted value	Model A	20.3	23.6	15.3	22.9	11.9	5.2	0.0	0.7	0.0	1.5
		Model B	19.1	18.1	15.8	19.2	10.4	7.2	0.0	9.8	0.0	4.0
50	Predicted value	Model A	20.7	22.8	16	23.2	10.5	5.8	0.0	0.9	0.0	1.6
		Model B	17.5	18.8	14.7	19.9	10.5	6.1	0.0	11.9	0.0	4.6
P	Predicted value	Model A	19.1	23.6	16.5	22.3	12	6.4	0.0	0.0	0.0	1.7
		Model B	18.5	21.9	18.6	18.4	10.3	6.5	0.0	2.3	3.5	2.7

RIs in the libraries used. In fact, their cross-entropy errors exceeded 1.6, whereas the errors in this work did not exceed 0.9, meaning that the error increases with an increase in the number of target RIs. Although there are several applications that utilize no prior information of the RIs contained in a given spectrum, some applications do have situations where the existing RIs may be predetermined. For example, some gamma-emitting RIs such as ^{152}Eu, ^{154}Eu, ^{54}Mn, ^{60}Co, ^{134}Cs, and ^{137}Cs are well documented for surveys of sites and for building characterizations as part of decommissioning works [28]. These RIs also exist in the form of check sources so that measurement-based base spectra are created. Another option is to construct an additional ANN that can distinguish target RIs from non-target RIs prior to the use of an ANN that analyzes a limited number of target RIs for a more accurate analysis of complex low-resolution spectra.

5. Conclusion

In this study, we presented two different ANNs trained by simulated spectra and trained by synthetic spectra, and these results were compared with each other for a quantitative analysis. From these results, we demonstrated how important it is to create training spectra which are as similar as possible to the measured spectra in terms of the accuracy of RI identification and the quantitative analysis outcomes. In this regard, a training set consisting of simulated spectra can degrade the accuracy when evaluating measured spectra. In addition, we showed that the model trained with synthetic spectra similar to the measured spectra did exhibit high accuracy in a quantitative analysis, even under low-count and gain-shift scenarios. Thus, these results suggest the feasibility of using a NaI(Tl) detector for the purpose of a quantitative analysis given that limitations such as the low resolution and the temperature dependency of the gain for some applications can be overcome.

Although our method and those in previous studies have shown promising results in analyzing complex low-resolution spectra, they provide only point estimates, possibly leading to overly confident decisions regardless of the degree of statistical variation present in the spectra. We are currently in the process of utilizing Bayesian inference to resolve this issue, and these results will be published as future work.

Acknowledgments

This work was supported by the Industrial Strategic Technology Development Program (10080094, Development of Specialized Equipment for Disaster and Public Safety Multicopter) funded by the Ministry of Trade, Industry & Energy (MOTIE, Korea).

References

[1] C.J. Sullivan, M.E. Martinez, S.E. Garner, Wavelet analysis of sodium iodide spectra, IEEE Nucl. Sci. Symp. Conf. Rec. 1 (2005) 302–306, http://dx.doi.org/10.1109/NSSMIC.2005.1596258.
[2] R.J. Estep, C.W. McCluskey, B.A. Sapp, The multiple isotope material basis set (MIMBS) method for isotope identification with low-and medium-resolution gamma-ray detectors, J. Radioanal. Nucl. Chem. 276 (2008) 737–741, http://dx.doi.org/10.1007/s10967-008-0626-6.
[3] R.J. Estep, D.R. Mayo, Application of the multiple isotope material basis set (MIMBS) method of isotope identification to low energy gamma emitters, J. Radioanal. Nucl. Chem. 282 (2009) 877–881, http://dx.doi.org/10.1007/s10967-009-0206-4.
[4] M. Alamaniotis, A. Heifetz, A.C. Raptis, L.H. Tsoukalas, Fuzzy-logic radioisotope identifier for gamma spectroscopy in source search, IEEE Trans. Nucl. Sci. 60 (2013) 3014–3024, http://dx.doi.org/10.1109/TNS.2013.2265307.
[5] C.J. Sullivan, J. Stinnett, Validation of a Bayesian-based isotope identification algorithm, Nucl. Instrum. Methods Phys. Res. A 784 (2015) 298–305, http://dx.doi.org/10.1016/j.nima.2014.11.113.
[6] J. Stinnett, C.J. Sullivan, An automated isotope identification algorithm using Bayesian statistics, IEEE Nucl. Sci. Symp. Conf. Rec. (2013) 1–7, http://dx.doi.org/10.1109/NSSMIC.2013.6829487.
[7] C.M. Carlevaro, M.V. Wilkinson, L.A. Barrios, A genetic algorithm approach to routine gamma spectra analysis, J. Instrum. 3 (2008) http://dx.doi.org/10.1088/1748-0221/3/01/P01001.
[8] M. Alamaniotis, J. Mattingly, L.H. Tsoukalas, Pareto-optimal gamma spectroscopic radionuclide identification using evolutionary computing, IEEE Trans. Nucl. Sci. 60 (2013) 2222–2231, http://dx.doi.org/10.1109/TNS.2013.2260869.
[9] M. Alamaniotis, T. Jevremovic, Hybrid fuzzy-genetic approach integrating peak identification and spectrum fitting for complex gamma-ray spectra analysis, IEEE Trans. Nucl. Sci. 62 (2015) 1262–1277, http://dx.doi.org/10.1109/TNS.2015.2432098.
[10] M. Kamuda, J. Stinnett, C.J. Sullivan, Automated isotope identification algorithm using artificial neural networks, IEEE Trans. Nucl. Sci. 64 (2017) 1858–1864, http://dx.doi.org/10.1109/TNS.2017.2693152.
[11] M. Kamuda, C.J. Sullivan, An automated isotope identification and quantification algorithm for isotope mixtures in low-resolution gamma-ray spectra, Radiat. Phys. Chem. 155 (2019) 281–286, http://dx.doi.org/10.1016/j.radphyschem.2018.06.017.
[12] M. Kamuda, J. Zhao, K. Huff, A comparison of machine learning methods for automated gamma-ray spectroscopy, Nucl. Instrum. Methods Phys. Res. A (2018) http://dx.doi.org/10.1016/j.nima.2018.10.063.
[13] V.M. Hernandez-Davila, T.G. Soto-Bernal, H.R. Vega-Carrillo, Determination of neutron fluence-to-dose conversion coefficients by means of artificial neural networks, Appl. Radiat. Isot. 83 (2014) 249–251, http://dx.doi.org/10.1016/j.apradiso.2013.04.014.
[14] E. Ronchi, P.A. Söderström, J. Nyberg, E. Andersson Sundén, S. Conroy, G. Ericsson, C. Hellesen, M. Gatu Johnson, M. Weiszflog, An artificial neural network based neutron-gamma discrimination and pile-up rejection framework for the BC-501 liquid scintillation detector, Nucl. Instrum. Methods Phys. Res. A 610 (2009) 534–539, http://dx.doi.org/10.1016/j.nima.2009.08.064.
[15] J. Jiang, P. Trundle, J. Ren, Medical image analysis with artificial neural networks, Comput. Med. Imaging Graph. 34 (2010) 617–631, http://dx.doi.org/10.1016/j.compmedimag.2010.07.003.
[16] X.H. Yu, G.A. Chen, Efficient backpropagation learning using optimal learning rate and momentum, Neural Netw. 10 (1997) 517–527, http://www.sciencedirect.com/science/article/pii/S0893608096001025%0Ahttp://www.scopus.com/scopus/inward/record.url?eid=2-s2.0-0031127257&partnerID=40.

[17] D.P. Kingma, J. Ba, Adam: A method for stochastic optimization, Int. Conf. Learn. Represent. (2015) 1–15, http://dx.doi.org/10.1145/1830483.1830503, arXiv:1412.6980v9.

[18] N. Srivastava, G. Hinton, A. Krizhevsky, I. Sutskever, R. Salakhutdinov, Dropout: A simple way to prevent neural networks from overfitting, J. Mach. Learn. Res. 15 (2014) 1929–1958, http://dx.doi.org/10.1214/12-AOS1000.

[19] François Chollet, et al., Chollet, Keras, GitHub, 2015. https://github.com/fchollet/keras.

[20] B. Jeon, J. Kim, M. Moon, G. Cho, Parametric optimization for energy calibration and gamma response function of plastic scintillation detectors using a genetic algorithm, Nucl. Instrum. Methods Phys. Res. A 930 (2019) 8–14, http://dx.doi.org/10.1016/j.nima.2019.03.003.

[21] Z.M. Wang, Y.H. Yu, Z.Y. Sun, K. Yue, D. Yan, Y.J. Zhang, Y. Zhou, F. Fang, W.X. Huang, J.L. Chen, Temperature dependence of the plastic scintillator detector for DAMPE, Chinese Phys. C. 41 (2017) 3–9, http://dx.doi.org/10.1088/1674-1137/41/1/016001.

[22] J. Snoek, H. Larochelle, R.P. Adams, Practical Bayesian optimization of machine learning algorithms, in: NIPS Proc., 2012, pp. 1–9. arXiv:1206.2944v2.

[23] J. Bergstra, Y. Bengio, Random search for hyper-parameter optimization, J. Mach. Learn. Res. 13 (2012) 281–305, http://dx.doi.org/10.1162/153244303322533223.

[24] J. Kim, K. Park, G. Cho, Multi-radioisotope identification algorithm using an artificial neural network for plastic gamma spectra, Appl. Radiat. Isot. 147 (2019) 83–90, http://dx.doi.org/10.1016/j.apradiso.2019.01.005.

[25] C.M. Salgado, L.E.B. Brandão, R. Schirru, C.M.N.A. Pereira, C.C. Conti, Validation of a NaI(Tl) detector's model developed with MCNP-X code, Prog. Nucl. Energy. 59 (2012) 19–25, http://dx.doi.org/10.1016/j.pnucene.2012.03.006.

[26] M.T. Hajheidari, M.J. Safari, H. Afarideh, H. Rouhi, Experimental validation of response function of a NaI (Tl) detector modeled with Monte Carlo codes, J. Instrum. 11 (2016) http://dx.doi.org/10.1088/1748-0221/11/06/p06011, P06011–P06011.

[27] C. Kim, Y. Kim, M. Moon, G. Cho, Iterative Monte Carlo simulation with the Compton kinematics-based GEB in a plastic scintillation detector, Nucl. Instrum. Methods Phys. Res. A 795 (2015) 298–304, http://dx.doi.org/10.1016/j.nima.2015.06.007.

[28] U.S. nuclear regulatory commission, multi-agency radiation survey and site investigation manual (MARSSIM), NUREG-Series, 2000, 2000, pp. 1–360, http://dx.doi.org/10.2172/569107.